MOX-Report No. 73/2024

Using SAR Data as an Effective Surrogate for Optical Data in Nitrogen Variable Rate Applications: a Winter Wheat Case Study

Liverotti, L.; Ferro, N.; Soli, L.; Matteucci, M.; Perotto, S.

MOX, Dipartimento di Matematica
Politecnico di Milano, Via Bonardi 9 - 20133 Milano (Italy)

mox-dmat@polimi.it https://mox.polimi.it

Using SAR Data as an Effective Surrogate for Optical Data in Nitrogen Variable Rate Applications: a Winter Wheat Case Study

Luca Liverotti[1], Nicola Ferro[1],
Luca Soli[2], Matteo Matteucci[3], Simona Perotto[2]

October 7, 2024

[1] MOX-Department of Mathematics, Politecnico di Milano, Piazza Leonardo da Vinci 32, Milan, 20133, MI, Italy; {luca.liverotti, nicola.ferro, simona.perotto}@polimi.it
[2] Thales Alenia Space S.p.A. Italia, Via E. Mattei 1, I-20064 Gorgonzola, MI, Italy; Luca.Soli@thalesaleniaspace.com
[3] Department of Electronics, Information and Bioengineering, Politecnico di Milano, Piazza Leonardo da Vinci 32, Milan, 20133, MI, Italy; matteo.matteucci@polimi.it

Abstract

This study highlights the feasibility of using SAR data as a surrogate for optical acquisitions in the generation of nitrogen prescription maps in wheat cultivation. Unlike the optical-based approaches which are negatively affected by adverse meteorological conditions, the proposed strategy provides the possibility to compute the fertilization maps at any date, by exploiting the all-weather, day-and-night SAR capabilities. We train a U-Net-like CNN architecture on Sentinel-2 optical and Sentinel-1 SAR datasets, after a properly alignment in time. The trained model returns a surrogate NDVI distribution starting from SAR acquisitions, when optical data are not available. The recovered NDVI information is converted into LAI and GAI distributions, by resorting to an exponential and a linear law, respectively, according to the literature. Finally, the nitrogen prescription map is obtained out of the recovered GAI values. A qualitative and quantitative analysis of the error between the optical and SAR-derived prescription maps shows that the procedure is accurate, especially during the tillering and the stem elongation growth phases.

1 Introduction

The life cycle of a plant is characterized by a sequence of visually observable phases, called phenological phases. The sequence of phenological phases is

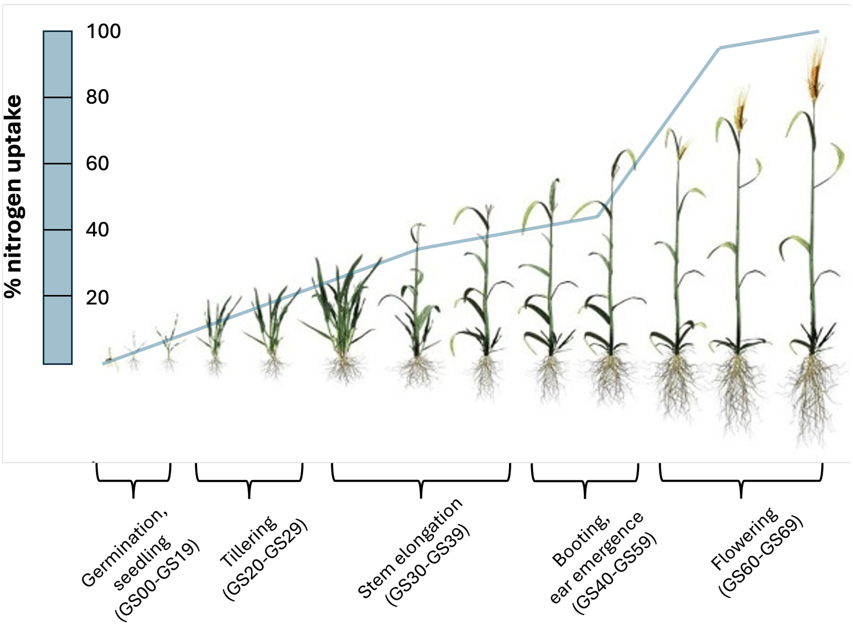

Figure 1: Sketch of the main wheat phenological stages and trend of the corresponding nitrogen uptake.

predetermined genetically, while the speed of phase succession is regulated by environmental factors and in particular by meteorological and hydrological ones (e.g., temperature, solar radiation, soil water content). The knowledge of phenological phases is fundamental for different agricultural practices, such as phytosanitary treatments, fertilization, irrigation, since they are effective only if carried out at specific phenological stages.

In this paper, we focus on winter wheat cultivation with a specific interest in optimization of fertilizer supply, in particular the nitrogen (N). Figure 1 shows the main wheat phenological stages together with the trend of nitrogen uptake during the growing season. It is customary to codify the different Growth Stages (GS) with a value ranging from 0 (for germination) to 99 (for flowering) [1]. The timing of nutrient intake is crucial, because it allows to maximize the yield and minimize the waste. Every nitrogen intake has a specific purpose and takes place at specific phenological stages. The first intake is minimal and is meant to stimulate the vegetative resumption. The second intake amounts to about a quarter of the total nitrogen need and it is provided during the tillering stage. The third intake is the most substantial one and it is supplied during the stem elongation phase, directly affecting the number of grains per spike and the size of grains. The fourth intake is necessary only for durum and bread making wheat and it is provided during the advanced booting phase. The wheat plant takes up the applied nitrogen and transfers it to the grains, where it is stored as proteins. Table 1 provides the typical amount of nitrogen associated with 4 distinct intakes.

Table 1: Nitrogen intakes related to a wheat crop.

	1^{st} **intake**	2^{nd} **intake**	3^{rd} **intake**	4^{th} **intake**
Nitrogen	20 kg ha^{-1}	40-60 kg ha^{-1}	60-100 kg ha^{-1}	40-50 kg ha^{-1}

However, following a calibrated nitrogen application is critical from an environmental impact perspective [2]. Indeed, an abuse of chemical fertilizer combined with a uniform spread across the field leads to an excess of soil nutrients that poison air and water (see Figure 2). Regarding air pollution, the nitrogen that is not absorbed by plants interacts with the soil, which releases nitrous oxide (N_2O) - a greenhouse gas - in the atmosphere, thus contributing to climate change. For instance, in 2017, N_2O emissions from agriculture have accounted for the 3.9% of total anthropogenic emissions in the European Union [3]. Water pollution arises from nitrogen leaching when soil becomes overly saturated from heavy rainfall. Prolonged precipitation causes excess nitrogen, not absorbed by plants, to wash away. This leached nitrogen can reach groundwater or water bodies, leading to significant environmental damage by promoting algae growth and depleting oxygen levels (eutrophication). Runoff of just 20 to 30 kg of nitrogen per hectare (200-300 g per 100 m^2) can elevate groundwater nitrate levels above the safe drinking water threshold of 50 mg per liter [4].

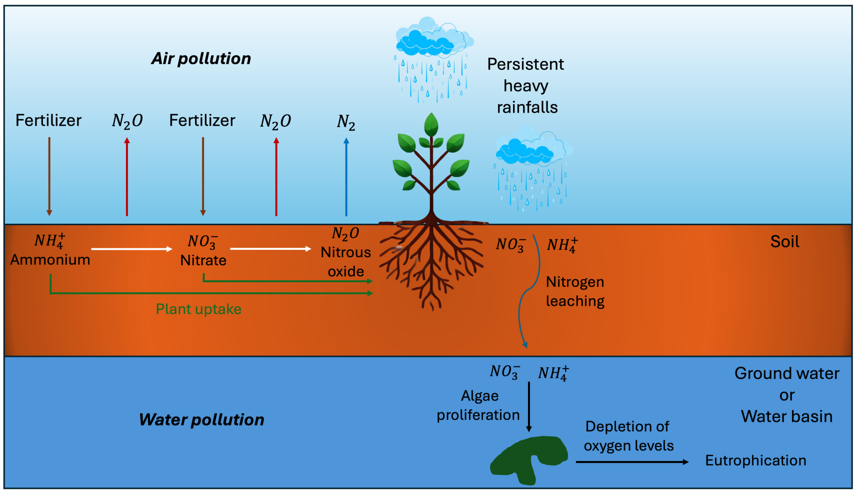

Figure 2: Sketch of air and water pollution due to nitrogen exceedings.

A possible solution to the pollution issue is given by Variable Rate Applications (VRA). In general, this term refers to the technology used in precision agriculture that allows for the variable application of resources such as seeds, fertilizers, and pesticides across a field. This approach addresses the specific needs and conditions of different parts of a field, aiming to optimize resource use and improve crop yields. VRA is usually implemented using map-based systems, based on pre-determined prescription maps. This technology reduces waste thus minimizing the environmental impact. In particular, such prescription maps are referred to as fertilization maps when dealing with nitrogen VRA (NVRA). NVRA maps are georeferenced matrices where each pixel represents a specific land plot, indicating the optimal nitrogen fertilizer amount needed. It has been proven that NVRA is able to reduce leached nitrogen amount up to 75% with respect to a uniform application [5].

The nitrogen nutritional status of cultivations can be monitored through remote sensing, which primarily relies on regions of the optical spectrum that include green, red, red-edge, near- and mid-infrared. Spectral bands are often combined with algebraic formulas to evaluate multiple vegetation indices (VI), used to assess crop parameters, such as vegetation status and chlorophyll content [6, 7, 8, 9, 10]. Among these indicators, the normalized difference vegetation index (NDVI), which measures the normalized difference between the reflectance of red and near-infrared (NIR) bands [11], is widely used to evaluate soil cover, leaf area, chlorophyll content, plant nitrogen nutritional status [12, 13, 14, 15, 16, 17, 18]. In particular, NDVI has been successfully employed to assess the nitrogen nutritional status of wheat in [19, 20, 21]. NDVI is also instrumental to compute the Leaf Area Index (LAI) - the ratio of total leaf surface to ground area - measuring the density of leaf coverage in a field (i.e., the health and productivity of the crop), as well as the Green Area Index (GAI) - the ratio of total green surface to ground area - measuring the occupation of leaves, stems, flowers (i.e., the plant photosynthetic activity).

To calculate NDVI in practice it is customary to leverage optical satellite data [22, 23, 24, 25, 26, 27]. In particular, the study in [22] predicts wheat nitrogen requirements using a two-step approach. First, yield is estimated with Machine Learning (ML) models like Random Forest and Generalized Additive Models, based on explanatory variables including soil characteristics (e.g., soil organic matter, pH, electrical conductivity) and remote sensing indices such as Normalized Difference Red Edge (NDRE) and NDVI. Then, the optimal nitrogen rate is determined by maximizing crop profit, which depends on the estimated yield.
Another notable nitrogen fertilization approach is the AgroSat model [23, 24], an open platform for precision agriculture in Italy. Developed by the National Research Council in 2017 as a Copernicus use case, AgroSat generates nitrogen prescription maps based on user input for nitrogen units and fertilizer content [25]. The model uses crop and sowing data, along with NDVI trends, applying an exponential function to relate NDVI to nitrogen rates. This function is derived from a broader model incorporating NDVI,

Figure 3: Google Maps satellite image of the study site, where the soft wheat cropland is identified by the yellow polygon.

the Nitrogen Nutrition Index (NNI), the chlorophyll red-edge index, and laboratory analyses like leaf nitrogen content.
The Agricolus model generates nitrogen prescription maps using Sentinel-2 satellite data - yield, weather, soil information [26, 27]. It bases nitrogen fertilization doses on the latest NDVI from Sentinel-2 and the field's average nitrogen needs calculated by the balance model. Soil texture (sand, silt, clay) and satellite indices are compared across years to spatialize the nitrogen rate. The tool allows users to compare crop vigor, chlorophyll content, and water stress indices, while an algorithm classifies pixels into homogeneous zones based on standard deviation from the mean.

The limitation of the optical data-based fertilization models is the scarce availability of acquisitions, for instance in the presence of unfavorable weather conditions. To address this issue, we propose a data fusion technique combining optical and Synthetic Aperture Radar (SAR) data, leveraging SAR's ability to provide all-weather, day-and-night information. The proposed approach consists of the following steps (see the workflow in the bottom part of Figure 4):

i) starting from optical and SAR data, train a U-Net-like Convolutional Neural Network (CNN) that learns the relationship between SAR backscatter coefficients and NDVI [28];

ii) exploit the model in i) to surrogate the optical NDVI information (when not available) from SAR data and compute the LAI and GAI maps, by resorting to well-consolidated correlation laws bewteen NDVI and LAI [29], and LAI and GAI;

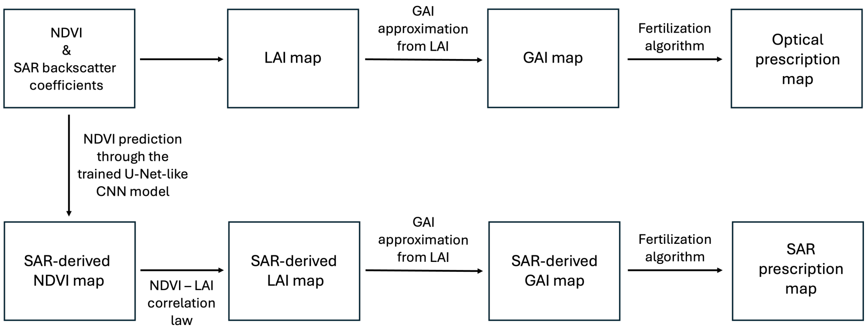

Figure 4: Workflow of the computation of optical (top) and SAR (bottom) prescription maps.

iii) construct the nitrogen prescription map by replacing optical with SAR-surrogate GAI values in established fertilization models [30].

A quantitative comparison between the original optical nitrogen prescription maps and their SAR-derived counterparts is conducted.

The paper is structured as follows. Section 2 provides the materials and the methods involved in the training of the U-Net-like CNN model and details the algorithm for the generation of the SAR nitrogen prescription map. In Section 3, we focus on the numerical validation of the predictive model both from a qualitative (fertilization maps) and quantitative (associated error analysis) viewpoint. The obtained results are discussed in Section 4. Finally, in the last section, we draw some conclusions and propose future research perspectives.

2 Materials and Methods

In this section we illustrate the materials and the methods involved in the experimentation about SAR-based surrogates of optical prescription maps. Optical data enables the direct computation of vegetation indices, including normalized difference vegetation index (NDVI), leaf area index (LAI), and green area index (GAI) (see the workflow in the upper part of Figure 4). However, this computation is often constrained by limited data availability, particularly during unfavorable weather conditions. In contrast, SAR acquisitions can be performed in all weather conditions, day or night, but they do not provide direct measurements of vegetation indices. This limitation underscores the need for the procedure detailed in this section.

2.1 Study area

We select as agricultural area of interest the soft wheat cropland yellow-highlighted in Figure 3, near the small town Trecella, 30 km east of Milan. It coincides with POLYGON (9.501835 45.520515, 9.483398 45.520515, 9.483398 45.508303, 9.501835 45.508303, 9.501835 45.520515) in WKT (well-known text) format, covering a surface of about 8 ha. The crop was monitored by using optical Sentinel-2 data over the last two growing seasons (2022-2023, 2023-2024) in the period between October (sowing stage) and July (harvest stage). The two panels in Figure 5 show the average NDVI and LAI trend of the wheat crop over the two growing seasons, while Figure 6 provides the associated availability of information about weather conditions in terms of cloudiness.

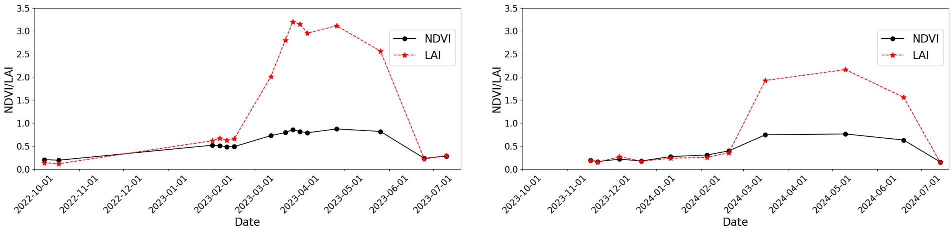

(a) (b)

Figure 5: Average NDVI and LAI trend of the monitored soft wheat cropland in Figure 3 over the growing seasons 2022-2023 (a), 2023-2024 (b).

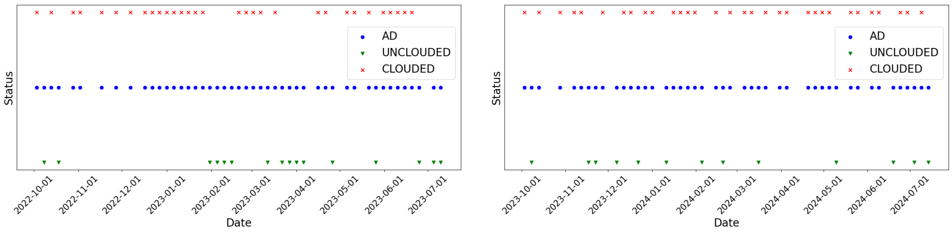

(a) (b)

Figure 6: Available data (AD) about weather conditions classified in terms of clouded or unclouded status over the soft wheat cropland over the growing seasons 2022-2023 (a), 2023-2024 (b).

2.2 Satellite Data

The SAR and optical data used for the experimentation have been collected by Sentinel-1 [31] and Sentinel-2 [32] satellite constellations, characterized by a 6- and 5-day revisit time, respectively. Sentinel-1 data provide dual vertical polarization (VV+VH) backscatter coefficients, $\Sigma = (\sigma_{VV}, \sigma_{VH})$, while Sentinel-2 collects wide swath high-resolution multispectral images with 13 optical spectral bands. Concerning Sentinel-1 we adopt the Interferometric Wide (IW) swath operational mode since it preserves revisit performance requirements and builds up a consistent long-term archive. In particular, we choose Ground Range Detected (GRD) High (H) spatial resolution - 20 meters - products, where pixel values represent the detected backscatter magnitude with reduced speckle, while no phase information is provide since useless for our analysis. Regarding Sentinel-2, we select Level-2A (L2A) products which provides orthorectified Surface Reflectance, considering bands with 10 meter spatial resolution. Both Sentinel-1 and Sentinel-2 data are processed using the SeNtinel Application Platform (SNAP) software [33]. Successively, theses data will be properly combined for training the U-Net-like CNN to approximate the NDVI map independently of weather conditions (see Section 2.3).

2.3 NDVI recovery from SAR data

NDVI is computed directly from optical data when available. Here, we focus on the method used to estimate NDVI when weather prevents optical data acquisition. To this aim, we generalize the approach in [28] to the agricultural context, by resorting to neural networks properly trained on both optical and SAR data. Throughout the paper, we adopt the notation NDVI_o for the optical measurement and NDVI_S for the SAR surrogate to distinguish the different origins, and analogously for indices LAI and GAI.

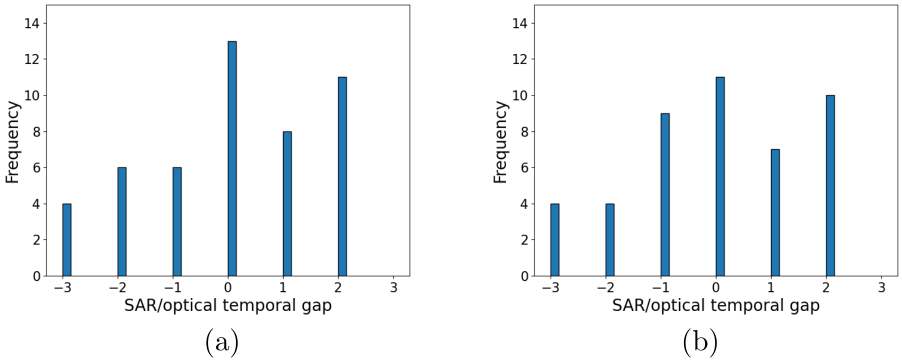

(a)

(b)

Figure 7: Frequency plot of the acquisition-date gap of the Sentinel-1/Sentinel-2 dataset over the growing seasons 2022-2023 (a), 2023-2024 (b).

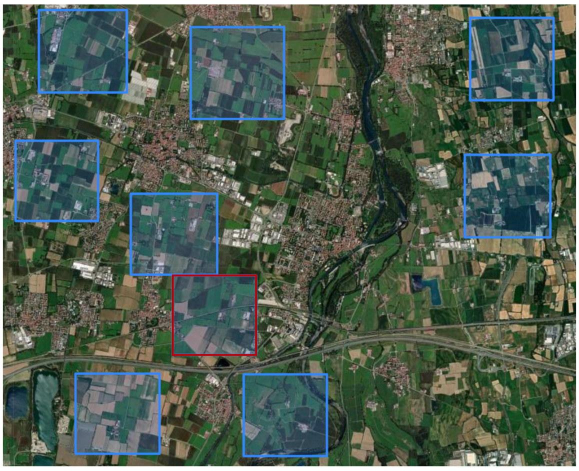

Figure 8: Satellite view of the patches used for the construction of the training/validation/test sets used to learn how derive NDVI from SAR backscatter. Red patch refers to the one in Figure 3 covering the wheat cropland.

2.3.1 The datasets

To train the neural network, we build a time-aligned Sentinel-1/Sentinel-2 dataset, similarly to [28]. We consider the SAR/optical data pairs, (Σ, NDVI_o), of SAR backscattered coefficients and measured NDVI, with a maximum acquisition-date gap of 3 days and no cloud cover. Figure 7 shows the frequency of the acquisition-date gap of the Sentinel-1/Sentinel-2 dataset for the considered growing seasons.

In particular, the SAR/optical data pairs are extracted from an area wider than the one in Figure 3 in order to create a sufficiently rich training set. To this aim, we consider the WKT string POLYGON(9.448694 45.492637, 9.567333 45.492637, 9.567333 45.561565, 9.448694 45.561565, 9.448694 45.492637) in Figure 8. Thus, for each SAR/optical data pair, we extract nine 128 × 128 px patches - with a pixel spacing equal to 10 m × 10 m - one (the red highlighted) including the wheat field, the remaining patches (the blue highlighted) located outside the crop of interest and covering purely agricultural areas. For each patch, we retrieve four coregistered maps , corresponding to NDVI_o, LAI_o, and the SAR backscatter coefficients in Σ (see Figure 9 for an example).

Regarding NDVI, the negative values are clipped to zero, since dealing with agricultural areas characterized by positive NDVI. SAR data are clipped to remove outliers and anomalous sensor values by thresholding VH and VV backscatter coefficients to the ranges [-32.5 dB, 0 dB], [-25 dB, 0 dB], respectively as in [28], and successively scaled to $[0, 1]$.

We consider two distinct Sentinel-1/Sentinel-2 time-aligned datasets, corresponding to different dates. The first one, referred to as the fertiliza-

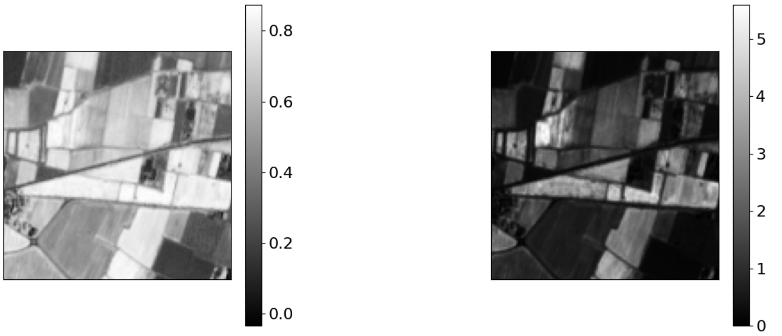

(a) NDVI$_o$ (b) LAI$_o$

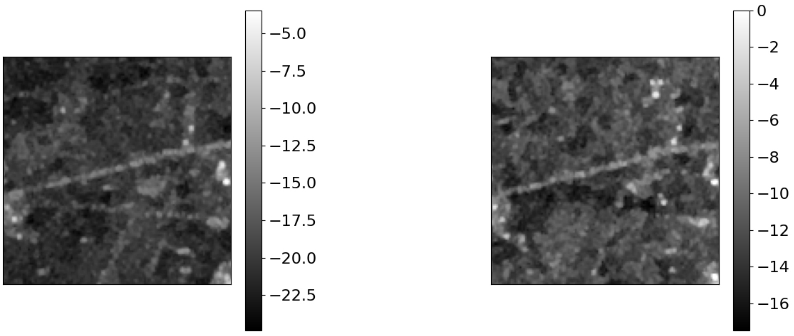

(c) σ_{VH} (d) σ_{VV}

Figure 9: Example of coregistered maps for the test patch, which covers the wheat crop, acquired from the SAR/optical data pair 23-02-10/23-02-09 (stem elongation stage).

tion dataset, considers the tillering and stem elongation stages - the period between January and March - over the growing seasons 2022-2023 and 2023-2024. The second dataset, named seasonal dataset, is broader spanning the period from February 2023 to June 2024. Table 2 shows the selected data pairs for the two datasets.

2.3.2 The U-Net-like CNN model and the training procedure

To estimate NDVI when weather conditions hinder the acquisition of optical data, we employ a variant of a standard U-Net architecture as in [28]. The U-Net is a widely recognized model for tasks like semantic segmentation and pixel-level regression, and it is frequently applied in remote sensing [34]. The U-Net is composed of an encoder and a decoder. The encoder is responsible for extracting essential features by reducing the spatial resolution of the input, which, in our case, are SAR backscatter values, through convolutional filters. The decoder reconstructs the NDVI values from the features thus

Table 2: SAR/optical time-aligned dates for the fertilization and seasonal datasets.

Fertilization dataset	**Seasonal dataset**
2023-02-01/2023-01-31	2023-02-08/2023-02-05
2023-02-08/2023-02-05	2023-03-09/2023-03-12
2023-02-09/2023-02-10	2023-05-27/2023-05-26
2023-02-13/2023-02-15	2023-07-15/2023-07-15
2023-03-09/2023-03-12	2023-10-07/2023-10-08
	2023-11-23/2023-11-22
2024-01-11/2024-01-11	
2024-02-04/2024-02-05	2024-01-11/2024-01-11
2024-02-20/2024-02-20	2024-02-04/2024-02-05
2024-03-15/2024-03-16	2024-03-15/2024-03-16
	2024-06-19/2024-06-19

extracted. To maintain spatial accuracy, skip connections are incorporated between the encoder and decoder, which help retain high-frequency details. Unlike the original U-Net design, which produces two probability maps without an activation function, we utilize a single output channel with a sigmoid activation function. This ensures that the model output, namely the predicted NDVI, takes value in the standard range $[0, 1]$. Additionally, in order to prevent checkerboard artifacts in the final image, in the decoder we replace up-convolutions with bilinear upsampling combined with standard convolutional layers [35].

For training the model, we opt for Mean Absolute Error (MAE) as the loss function, as it preserves more spatial detail compared to Mean Squared Error loss [36]. To evaluate the U-Net model and compare the prediction with the optical derived values, we use MAE metric, defined by

$$\text{MAE}(\text{NDVI}_S, \text{NDVI}_o) = \frac{1}{N} \sum_{i=1}^{N} |\text{NDVI}_S(i) - \text{NDVI}_o(i)|,$$

with $\text{NDVI}_S(i)$ and $\text{NDVI}_o(i)$ the surrogate and the optical measured NDVI for the i-th pixel, respectively, for $i = 1, \ldots, N$.

With reference to the employed data, for the training and validation phase, we consider the blue-highlighted patches in Figure 8 and we randomly shuffle the corresponding patch list. In more detail, the first 20% of the items in the patch list forms the validation set, while the remaining 80% constitutes the training set. The testing is evaluated over the red-highlighted patch in Figure 8 - covering the wheat crop of interest - for the nine dates of the fertilization dataset in Table 2, since related to the main goal of the paper, namely the generation of fertilization maps.

Regarding the algorithmic specifics, the model is trained by using the Adam optimiser [37], with an initial learning rate of 0.001. As learning rate scheduling, we halve the learning rate every 8 epochs, for a total of 50 epochs. For each epoch, the MAE of the validation set is computed so that, if there is an improvement with respect to the previous best validation MAE value, the weights of the model are updated. The batch size is set to 8 for training and validation, to 1 for the testing.

2.4 LAI/GAI recovery from SAR data

The NDVI_S, output of the U-Net-like CNN model, is exploited to approximate the LAI distribution on the crop of interest. To this aim, we resort to the well-established correlation law between LAI and NDVI for herbaceous cultivations (see Figure 10, left panel)

$$LAI = 0.172\, \mathrm{e}^{3.64\, \mathrm{NDVI}}, \tag{1}$$

whose validity period ranges between the beginning of tillering and the ripening, though in the last one there is a low NDVI sensitivity to LAI variation due to the exponential nature of the correlation law [29]. Relation (1) is derived through a regression analysis - with a determination coefficient $r^2 = 0.91$, standard error equal to 0.5 - and provides us a SAR approximation, LAI_S, for LAI together with an associated map. Since during the tillering stage LAI is on average slightly smaller than GAI (see, e.g., [38, 39]), we compute the GAI_S distribution as a 10% increment of the LAI_S value for each pixel of the map (see Figure 10, right panel).

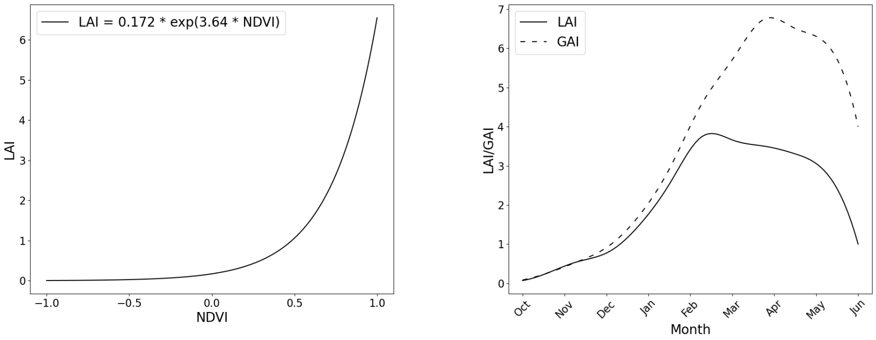

Figure 10: Plot of the law (1) between LAI and NDVI (left) and monthly trend for LAI and GAI (right) for herbaceous crops.

2.5 From GAI_S to the nitrogen prescription map

To commute the GAI_S values into a practical information coinciding with the fertilization map, we exploit the methodology introduced in [30] for winter wheat crops, based on the research in [40, 1]. The authors settle a strategy to ensure a target level, GAI^T, of the GAI before the flowering stage, starting from the pixel values, $\mathrm{GAI}(i)$, for $i = 1, \dots, N$, of the same index at the tillering stage (i.e., between January and February); the canopy nitrogen requirement, N_{CR} [kg ha^{-1}], namely the amount of nitrogen responsible for a GAI unitary increment in one hectar wheat crop; the Soil Mineral nitrogen, N_{SM} [kg ha^{-1}], supply, namely the amount of readily available nitrogen in the soil that plants can absorb for growth and development; the average recovery rate of the soil, R_{S} [%], which measures the percentage of nitrogen that are effectively taken up by plants from the soil. In particular, the following steps are to be carried out:

1. scale N_{CR} and N_{SM} with respect to the data spatial resolution, namely the pixel area A^P [px/ha], in order to determine the quantity $\mathrm{N}^P_{\mathrm{CR}} = \mathrm{N}_{\mathrm{CR}}/A^P$ [kg px^{-1}] and $\mathrm{N}^P_{\mathrm{SM}} = \mathrm{N}_{\mathrm{SM}}/A^P$ [kg px^{-1}] of nitrogen that yields one unit increment of GAI and that is readily available in the soil for pixel, respectively;

for each pixel i:

2. compute the missing units, $\Delta_{\mathrm{GAI}}(i) = \mathrm{GAI}^T$ - $\mathrm{GAI}(i)$, required to reach the target level;
3. determine the quantity of nitrogen, $\mathrm{N}_\Delta(i) = \Delta_{\mathrm{GAI}}(i)\,\mathrm{N}^P_{\mathrm{CR}}$ [kg px^{-1}], required to reach the target GAI^T;
4. update quantity $\mathrm{N}_\Delta(i)$ by taking into account the SMN supply, $\mathrm{N}_\Delta(i) \leftarrow \mathrm{N}_\Delta(i) - \mathrm{N}_{\mathrm{SM}}$ [kg px^{-1}];
5. compute the effective nitrogen requirement of the pixel, $\mathrm{N}^*_\Delta(i) = \mathrm{N}_\Delta(i)(1 - \mathrm{R}_{\mathrm{S}})/\mathrm{R}_{\mathrm{S}}$ [kg px^{-1}], by accounting for the average recovery rate of the soil;

6. build the nitrogen prescription map, N^*_Δ [kg px^{-1}], by collecting values $\mathrm{N}^*_\Delta(i)$ across the pixels, for $i = 1, \dots, N$.

Algorithm 1.-6. can be applied a priori to both GAI_o and GAI_S, depending on the available satellite data. For the specific goal of this section, GAI is identified with GAI_S.

Finally, we observe that prescription maps for various intakes (see Table 1) can be generated by distributing values from the initial map across the specified fertilization times, following standard agronomic guidelines. It is also recommended to recalculate the prescription map periodically and compare it to earlier versions in order to ensure the fertilization strategy remains accurate and effective based on current crop and soil conditions.

3 Results

In this section we present the results about the performance of the prediction model proposed in the previous section in terms of NDVI_S estimation and accuracy of the fertilization map with respect to the optical data. Both the datasets in Table 2 are used in this analysis.
With reference to the procedure 1.-6. in Section 2.5, we adopt the following values for the quantities involved [30]:

$$\mathrm{GAI}^T = 6.5,\ \mathrm{N_{CR}} = 35\,[\mathrm{kg\,ha^{-1}}],\ \mathrm{N_{SM}} = 75\,[\mathrm{kg\,ha^{-1}}],$$

$$\mathrm{R_S} = 60\%,\ A^P = 10 \times 10\,[\mathrm{px/ha}].$$

3.1 NDVI estimation

We train the model in Sec 2.3.2 on the two SAR/optical datasets in Sec 2.3.1, thus setting fertilization and seasonal model, respectively. In particular, the training phase is performed over all the blue-highlighted patches in Figure 8 at the time-aligned dates in Table 2. The test phase is carried out over the red-highlighted patch covering the wheat crop only for the nine dates constituting the fertilization dataset.

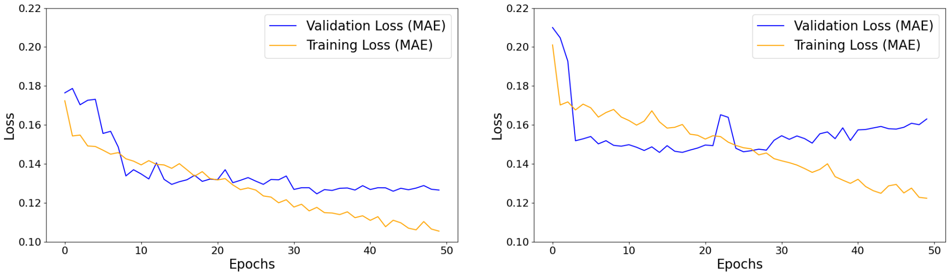

(a) (b)

Figure 11: Trend of the training and of the validation loss as a function of the number of epochs for the fertilization (a) and the seasonal (b) dataset.

Figure 11 shows the trend of the training and validation losses associated with the fertilization and seasonal models. The fertilization loss achieves a better validation performance. In particular, the best validation MAE value is reached at epoch 33 and 14 by the fertilization and the seasonal model, being equal to 0.125 and 0.146, respectively.

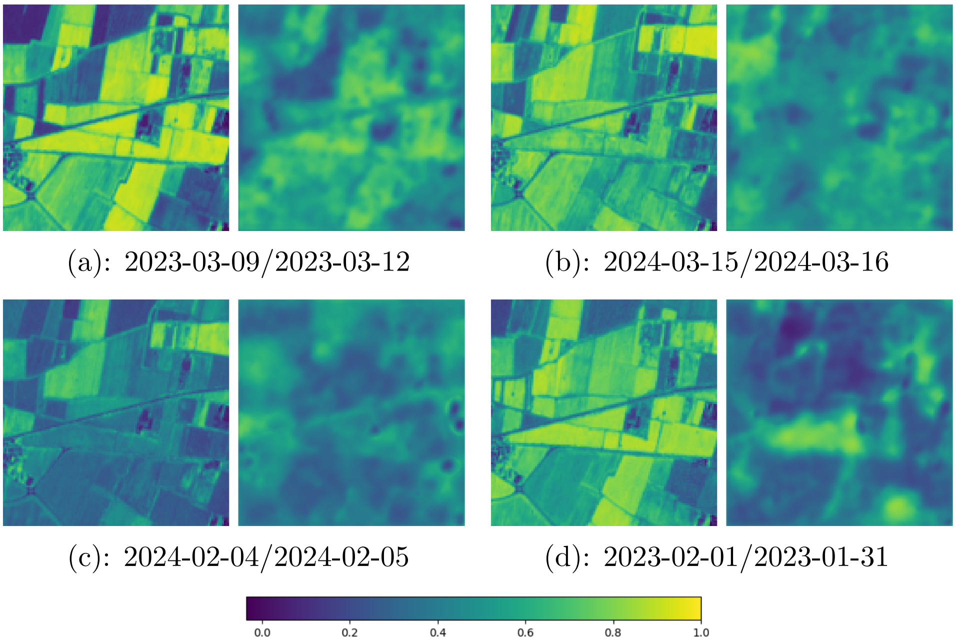
(a): 2023-03-09/2023-03-12

(b): 2024-03-15/2024-03-16

(c): 2024-02-04/2024-02-05

(d): 2023-02-01/2023-01-31

Figure 12: Comparison between the NDVI_o (left panels) and NDVI_S (right panels) distribution for the fertilization (top) and the seasonal (bottom) models: best (panels (a) and (c)) and worst (panels (b) and (d)) approximations.

Figure 12 is instrumental to evaluate the inference performance of the proposed method. It compares the distribution of NDVI_o (left panels) with NDVI_S (right panels) for the wheat crop field in Figure 8. The best (panels (a) and (c)) and worst (panels (b) and (d)) results are shown for the fertilization (top) and seasonal (bottom) model. We notice that the NDVI_S maps are particularly blurred, with a noticeable loss of spatial detail, when compared with the corresponding optical distribution, where crop boundaries are sharply defined. However, the best approximations in panels (a) and (c) preserve the main features, such as the two intersecting roads in the middle of the image, running from left to right. This loss of visual accuracy is, however, offset by the fact that these maps still manage to retain quantitative information as supported by the values in Table 3. Indeed, the average test MAE is almost the same for both the models, namely 0.167 for the fertilization model and 0.166 for the seasonal one, corresponding to a relative mean error around 16%. On the contrary, we highlight a significant difference in terms of MAE variability across the two models. The fertilization model exhibits a concentrated error distribution, ranging from 15% to 18% corresponding to a standard deviation equal to 1.2%; the seasonal model features a more spread distribution, from 11% to 25%, with a higher standard deviation which reaches the value 4.3%.

Table 3: Quantitative information related to the testing phase of both models in terms of MAE value $\mathrm{MAE}(\mathrm{NDVI}_S, \mathrm{NDVI}_o)$ associated with the red-highlighted patch in Figure 8.

SAR/optical time-aligned dates	**Fertilization model**	**Seasonal model**
2023-02-01/2023-01-31	0.170	0.255
2023-02-08/2023-02-05	0.171	0.209
2023-02-09/2023-02-10	0.163	0.148
2023-02-13/2023-02-15	0.176	0.201
2023-03-09/2023-03-12	0.150	0.131
2024-01-11/2024-01-11	0.151	0.129
2024-02-04/2024-02-05	0.183	0.116
2024-02-20/2024-02-20	0.158	0.151
2024-03-15/2024-03-16	0.186	0.151

Table 4: Quantitative information related to the testing phase of both models in terms of MAE value $\mathrm{MAE}_{\mathcal{C}}(\mathrm{NDVI}_S, \mathrm{NDVI}_o)$ associated with the polygonal area in Figure 3.

SAR/optical time-aligned dates	**Fertilization model**	**Seasonal model**
2023-02-01/2023-01-31	0.202	0.236
2023-02-08/2023-02-05	0.118	0.208
2023-02-09/2023-02-10	0.208	0.189
2023-02-13/2023-02-15	0.095	0.157
2023-03-09/2023-03-12	0.145	0.061
2024-01-11/2024-01-11	0.036	0.075
2024-02-04/2024-02-05	0.027	0.028
2024-02-20/2024-02-20	0.112	0.168
2024-03-15/2024-03-16	0.359	0.202

As a further check, in Table 4 we focus on the accuracy of the NDVI prediction confined to the wheat crop of interest (i.e., the polygonal area in Figure 3) by computing the mean absolute error

$$\mathrm{MAE}_{\mathcal{C}}(\mathrm{NDVI}_S, \mathrm{NDVI}_o) = \frac{1}{N_{\mathcal{C}}} \sum_{i \in \mathcal{C}} |\mathrm{NDVI}_S(i) - \mathrm{NDVI}_o(i)|, \tag{2}$$

with $\mathcal{C}$ the selected crop region and $N_{\mathcal{C}}$ the number of pixels belonging to $\mathcal{C}$. In this localized context, the performance of the SAR/optical approximation tool is improved for both the models, the relative mean error being now around 14%.

3.2 Comparison between optical and SAR prescription maps

The optical and SAR prescription maps, $\mathrm{N}^*_{\Delta,o}$ and $\mathrm{N}^*_{\Delta,\mathcal{S}}$, are computed through Algorithm 1.-6. when $\mathrm{GAI} = \mathrm{GAI}_o$ and $\mathrm{GAI} = \mathrm{GAI}_{\mathcal{S}}$, respectively, for both the datasets in Table 2.

To evaluate the accuracy of the SAR prescription map, we focus on the wheat crop area of interest in Figure 3 and we resort to the mean absolute error between the two fertilization maps, measured in [kg px^{-1}],

$$\mathrm{MAE}_{\mathcal{C}}(\mathrm{N}^*_{\Delta,\mathcal{S}}, \mathrm{N}^*_{\Delta,o}) = \frac{1}{N_{\mathcal{C}}} \sum_{i\in\mathcal{C}} |\mathrm{N}^*_{\Delta,\mathcal{S}}(i) - \mathrm{N}^*_{\Delta,o}(i)|, \tag{3}$$

and to the percentage relative error map, with a pixelwise value given by

$$\mathrm{Err}^{\%}_{\mathrm{N}^*_{\Delta}}(i) = \frac{|\mathrm{N}^*_{\Delta,\mathcal{S}}(i) - \mathrm{N}^*_{\Delta,o}(i)|}{\mathrm{N}^*_{\Delta,o}(i)} \cdot 100, \tag{4}$$

with $i = 1, \ldots, N_{\mathcal{C}}$.

In Tables 5, 6, we collect metrics $\mathrm{MAE}_{\mathcal{C}}(\mathrm{NDVI}_{\mathcal{S}}, \mathrm{NDVI}_o)$ in (2), the analogously defined value $\mathrm{MAE}_{\mathcal{C}}(\mathrm{LAI}_{\mathcal{S}}, \mathrm{LAI}_o)$, the quantity in (3), together with the aggregated indicators

$$\overline{\mathrm{NDVI}}_o = \frac{1}{N_{\mathcal{C}}} \sum_{i\in\mathcal{C}} \mathrm{NDVI}_o(i), \quad \overline{\mathrm{Err}^{\%}_{\mathrm{N}^*_{\Delta}}} = \frac{1}{N_{\mathcal{C}}} \sum_{i\in\mathcal{C}} \mathrm{Err}^{\%}_{\mathrm{N}^*_{\Delta}}(i), \tag{5}$$

related to the fertilization and seasonal datasets, respectively. In particular, the smallest and the largest errors associated with the SAR approximation are highlighted in bold.

A qualitative comparison between the optical (left panels) and the SAR (middle panels) nitrogen prescription maps is provided in Figures 13 and 14 for the fertilization and seasonal model, respectively, together with the corresponding relative percentage error map (right panels). Maps in the top (bottom) row refer to the best (worst) SAR approximation computed.

4 Discussion

We critically discuss the results presented in the Section 3.2.

From the values in Tables 5 and 6, it is evident that the SAR approximation is reliable to plan an effective fertilization strategy in January and February, the mean absolute and the percentage errors remaining low. This holds for both the fertilization and seasonal models. In particular, the values of $\mathrm{MAE}_{\mathcal{C}}(\mathrm{N}^*_{\Delta,\mathcal{S}}, \mathrm{N}^*_{\Delta,o})$ are very low, ranging from 0.05 to 0.18 [kg px^{-1}] (corresponding to a variation of percentage relative error from 2.77% to 9.57%)

and from 0.03 to 0.13 [kg px^{-1}] (corresponding to a variation of percentage relative error from 1.80% to 6.77%) of nitrogen for the fertilization and seasonal model, respectively.

Table 5: Performance of the SAR fertilization model in terms of metrics and aggregated indicators.

SAR/optical time-aligned dates	$\overline{\mathbf{NDVI}}_o$	$\mathbf{MAE}_{\mathcal{C}}$**(NDVI)**	$\mathbf{MAE}_{\mathcal{C}}$**(LAI)**	$\mathbf{MAE}_{\mathcal{C}}(\mathbf{N}^*_{\Delta})$	$\overline{\mathbf{Err}^{\%}_{\mathrm{N}^*_{\Delta}}}$
2023-02-01/2023-01-31	0.52	**0.202**	**0.08**	**0.05**	**2.77**
2023-02-08/2023-02-05	0.51	0.118	0.17	0.09	5.74
2023-02-09/2023-02-10	0.49	0.208	0.15	0.08	5.08
2023-02-13/2023-02-15	0.49	0.095	0.16	0.09	5.36
2023-03-09/2023-03-12	0.73	0.145	0.63	0.34	37.66
2024-01-11/2024-01-11	0.28	0.036	0.21	0.11	6.10
2024-02-04/2024-02-05	0.31	0.027	0.32	0.18	9.57
2024-02-20/2024-02-20	0.40	0.112	0.14	0.08	4.23
2024-03-15/2024-03-16	0.75	**0.359**	**1.21**	**0.66**	**70.61**

Table 6: Performance of the SAR seasonal model in terms of metrics and aggregated indicators.

SAR/optical time-aligned dates	$\overline{\mathbf{NDVI}}_o$	$\mathbf{MAE}_{\mathcal{C}}$**(NDVI)**	$\mathbf{MAE}_{\mathcal{C}}$**(LAI)**	$\mathbf{MAE}_{\mathcal{C}}(\mathbf{N}^*_{\Delta})$	$\overline{\mathbf{Err}^{\%}_{\mathrm{N}^*_{\Delta}}}$
2023-02-01/2023-01-31	0.52	0.236	0.13	0.07	4.31
2023-02-08/2023-02-05	0.51	0.208	0.18	0.10	6.22
2023-02-09/2023-02-10	0.49	0.189	0.14	0.08	4.54
2023-02-13/2023-02-15	0.49	0.157	0.10	0.05	3.19
2023-03-09/2023-03-12	0.73	**0.061**	**0.79**	**0.43**	**47.40**
2024-01-11/2024-01-11	0.28	0.075	0.12	0.07	3.52
2024-02-04/2024-02-05	0.31	0.028	0.23	0.13	6.77
2024-02-20/2024-02-20	0.40	**0.168**	**0.06**	**0.03**	**1.80**
2024-03-15/2024-03-16	0.75	0.202	0.63	0.35	37.06

This prediction is reasonable by considering that the quantity of fertilizer supplied in such a period is on average equal to 1.75 [kg px^{-1}].
On the contrary, the approximation capability of Algorithm 1.-6. turns out to be markedly less reliable in March, the mean absolute (and associated relative percentage) error reaching values 0.66 [kg px^{-1}] (70.61%) and 0.43 [kg px^{-1}] (47.40%) of nitrogen for the fertilization and seasonal model, respectively.

The deterioration of the SAR approximation for the March dates may be justified by the discrepancy between the GAI and LAI trends at the beginning of March (see Figure 10, right), making the GAI a less reliable proxy for the LAI from that period onward. The 10% correction applied to the GAI likely needs to be updated to higher values.

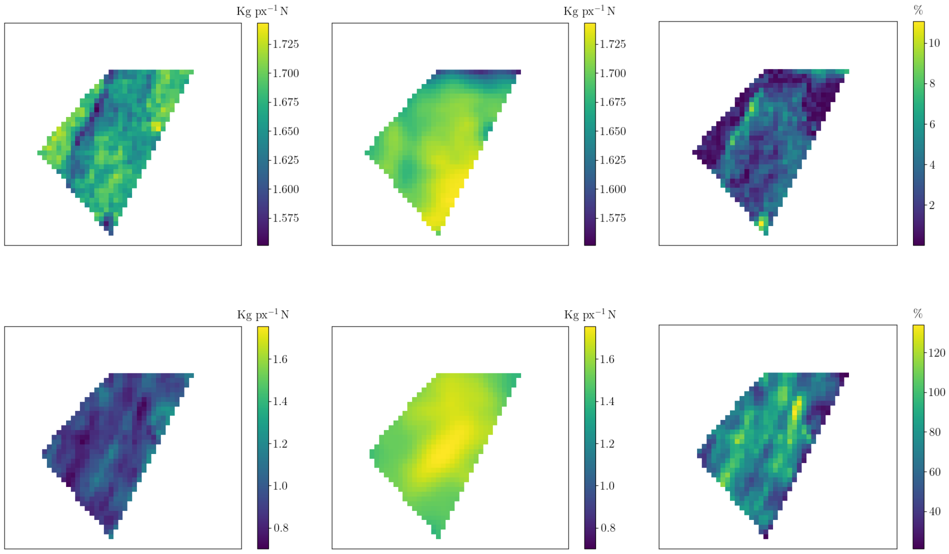

Figure 13: Comparison between the $\mathrm{N}^*_{\Delta,o}$ (left panels) and $\mathrm{N}^*_{\Delta,S}$ (middle panels) and associated relative percentage error distribution (right panels) for the best (top) and worst (bottom) SAR approximations with reference to the fertilization model.

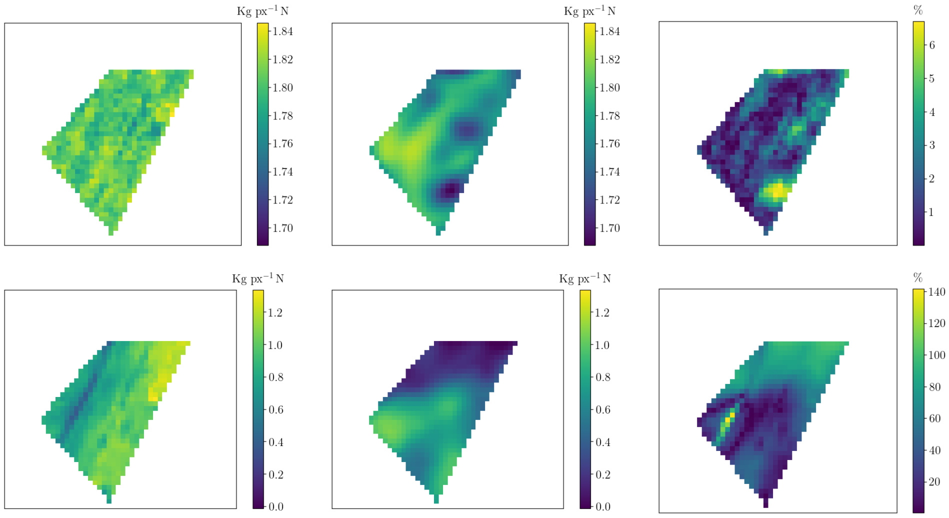

Figure 14: Comparison between the $\mathrm{N}^*_{\Delta,o}$ (left panels) and $\mathrm{N}^*_{\Delta,S}$ (middle panels) and associated relative percentage error distribution (right panels) for the best (top) and worst (bottom) SAR approximations with reference to the seasonal model.

An additional potential source of prediction error can be identified in the law mapping NDVI_S into LAI_S. In fact, when optical data is available, both NDVI_o and LAI_o can be directly calculated without relying on (1). In the absence of such data, it becomes necessary to use the exponential law, which will inevitably introduce an error, which is amplified for high NDVI_S values (see Figure 10, left). In particular, the closer $\overline{\mathrm{NDVI}_o}$ is to 1, the more the error is increased, leading to a greater deterioration in the accuracy of the LAI_S approximation. From the values in Tables 5 and 6, we observe that the SAR model is not fully reliable when $\overline{\mathrm{NDVI}_o} \geq 0.73$. For example, for the dates 2023-03-09/2023-03-12 and 2024-01-11/2024-01-11, the NDVI_S approximations exhibit similar accuracy, the values for $\mathrm{MAE}_{\mathcal{C}}(\mathrm{NDVI}_S, \mathrm{NDVI}_o)$ being 0.06 and 0.08, respectively. However, the exponential relationship between NDVI_S and LAI_S leads the corresponding $\mathrm{MAE}_{\mathcal{C}}(\mathrm{LAI}_S, \mathrm{LAI}_o)$ values to differ significantly, reaching 0.79 in correspondence with $\overline{\mathrm{NDVI}_o} = 0.73$, while attaining a lower value equal to 0.12 for $\overline{\mathrm{NDVI}_o} = 0.28$. To summarize, the low reliability of the fertilization map for March can be attributed both to the poor matching between LAI and GAI during this month and to the need to use the exponential law between LAI and NDVI in the absence of optical data.

As a final remark, we observe that the selected model (fertilization or seasonal) does not impact on the global trend of the adopted metrics and aggregated indicators. Indeed, the discrepancy between the relative percentage errors associated with the two models exhibits a minimal variation, ranging from 0.47% (2023-02-08/2023-02-05) to 2.8% (2024-02-04/2024-02-05) for each date in January and February. However, the seasonal approach is slightly preferable, outperforming the fertilization model on 5 out of the 7 dates within this period.

Concerning the maps in Figures 13-14, they suffer from the same blurred effect already observed in Figure 12 for the NDVI_S distributions, in contrast to the grainy appearance of the optical maps. Finally, the best approximations are characterized by a more homogeneous distribution of the error with respect to the worst predictions.

5 Conclusions and perspectives

The present study corroborates the feasibility of using SAR data as a surrogate for optical data for the computation of wheat nitrogen fertilization maps. The proposed approach addresses the limitations of methods entirely based on optical acquisitions (which may be unavailable, for instance, due to cloud cover) by leveraging SAR capabilities, specifically all-weather, day-and-night data availability. In particular, fertilization maps for dates lacking optical data are generated through a 3-step recovery process: i) we train a U-Net-like CNN model on optical/SAR data (NDVI/SAR backscatter coefficients), associated with properly time-aligned dates from a fertilization

(January-March 2022-2023, 2023-2024) and a seasonal (January-December 2022-2023, 2023-2024) dataset. This step allows to surrogate NDVI from SAR data for each day of interest in a target crop; ii) the surrogate NDVI is exploited to compute the LAI map through the exponential correlation law (1) together with the GAI distribution by exploiting a linear relationship between LAI and GAI; iii) Algorithm 1.-6. is used to generate the nitrogen prescription map.

We test the procedure on nine fertilization dates (January-March) over the two considered growing season. The key findings from our numerical experiments are:

- The accuracy of SAR-based prescription maps computed in January and February, using both the fertilization and seasonal approaches, is satisfactory, with the mean relative percentage error ranging from 1.8% to 9.57%. Furthermore, we note that, except for one data pair, all the relative percentage errors do not exceed 7% in the January and February;
- SAR-based prescription maps for March shows low accuracy for both the models, with mean relative percentage errors between 37.06% and 70.61%; this can be ascribed to the exponential correlation between NDVI and LAI and to the GAI/LAI adopted relationship;
- despite the two models yield comparable results, the seasonal one slightly outperforms the fertilization approach, providing better accuracy in 5 out of 7 dates during January and February.

A potential future direction for this work is the direct computation of LAI maps from SAR data, thus bypassing the derivation of LAI from NDVI (i.e., the use of an exponential law). Possible options in this context include an enhancement of the U-Net-like CNN model and the approaches proposed in [41] and [42].

Acknowledgments

L.L., N.F., S.P. are members of the Gruppo Nazionale Calcolo Scientifico–Istituto Nazionale di Alta Matematica (GNCS–INdAM). L.L., N.F. and S.P. acknowledge the support by MUR, grant Dipartimento di Eccellenza 2023–2027. M.M. acknowledges the support of Agritech National Research Center and received funding from the European Union Next-GenerationEU (PIANO NAZIONALE DI RIPRESA E RESILIENZA (PNRR) – MISSIONE 4 COMPONENTE 2, INVESTIMENTO 1.4 – D.D. 1032 17/06/2022, CN00000022).

References

[1] Agriculture and Horticulture Development Board (AHDB), *The wheat growth guide*, 2018.

[2] J. Martinez-Dalmau, J. Berbel, R. Ordonez-Fernandez, Nitrogen fertilization. a review of the risks associated with the inefficiency of its use and policy responses, Sustainability 13 (may 2021).

[3] European Commission, *Farm to Fork strategy*.
URL `https://food.ec.europa.eu/system/files/2020-05/f2f_action-plan_2020_strategy-info_en.pdf`

[4] M. H. Jeuffroy, B. Ney, A. Ourry, Integrated physiological and agronomic modelling of n capture and use within the plant, J. Exp. Bot. 53 (370) (2002) 809–823.

[5] Ministero delle Politiche Agricole Alimentari e Forestali (MIPAAF), *Linee guida per lo sviluppo dell'agricoltura di precisione in Italia* (2017).

[6] J. G. P. W. Clevers, L. Kooistra, M. M. M. van den Brande, Using Sentinel-2 data for retrieving LAI and leaf and canopy chlorophyll content of a potato crop, Remote Sens. 9 (405) (2017).

[7] A. Tassi, M. Vizzari, Object-Oriented LULC Classification in Google Earth Learning Algorithms, Remote Sens. (3776) (2020).

[8] N. G. Silleos, T. Alexandridis, I. Z. Gitas, K. Perakis, Vegetation Indices: Advances Made in Biomass Estimation and Vegetation Monitoring in the Last 30 Years, Geocarto Int. 21 (21–28) (2006).

[9] G. Messina, J. Peña, M. Vizzari, G. Modica, A Comparison of UAV and Satellites Multispectral Imagery in Monitoring Onion Crop. An Application in the 'Cipolla Rossa di Tropea' (Italy), Remote Sens. 12 (3424) (2020).

[10] J. Xue, B. Su, Significant Remote Sensing Vegetation Indices: A Review of Developments and Applications, J. Sens. 2017 (2017) 1–17.

[11] J. W. Rouse, R. H. Haas, J. A. Schell, D. W. Deering, Monitoring vegetation systems in the great plains with erts, Proc. ERTS-1 Symp. 1 (1974) 309–317.

[12] R. F. Muñoz-Huerta, R. G. Guevara-Gonzalez, L. M. Contreras-Medina, I. Torres-Pacheco, J. Prado-Olivarez, R. V. Ocampo-Velazquez, A Review of Methods for Sensing the Nitrogen Status in Plants: Advantages, Disadvantages and Recent Advances, Sensors 13 (2013) 10823–10843.

[13] L. Cabrera-Bosquet, G. Molero, A. Stellacci, J. Bort, S. Nogués, J. Araus, NDVI as a potential tool for predicting biomass, plant nitrogen content and growth in wheat genotypes subjected to different water and nitrogen conditions, Cereal Res. Commun. 39 (2011) 147–159.

[14] T. N. Carlson, D. A. Ripley, On the relation between NDVI, fractional vegetation cover, and leaf area index, Remote Sens. Environ. 62 (1997) 241–252.

[15] S. Stamatiadis, C. Christofides, C. Tsadilas, V. Samaras, J. S. Schepers, D. Francis, Ground-Sensor Soil Reflectance as Related to Soil Properties and Crop Response in a Cotton Field, Precis. Agric. 6 (2005) 399–411.

[16] P. Hansen, J. Schjoerring, Reflectance measurement of canopy biomass and nitrogen status in wheat crops using normalized difference vegetation indices and partial least squares regression, Remote Sens. Environ. 86 (2003) 542–553.

[17] T. Magney, J. U. Eitel, D. R. Huggins, L. A. Vierling, Proximal NDVI derived phenology improves in-season predictions of wheat quantity and quality, Agric. For. Meteorol. 217 (2016) 46–60.

[18] I. Herrmann, A. Pimstein, A. Karnieli, Y. Cohen, V. Alchanatis, D. Bonfil, LAI assessment of wheat and potato crops by VENμ S and Sentinel-2 bands, Remote Sens. Environ. 115 (2011) 2141–2151.

[19] S. R. Sultana, A. Ali, A. Ahmad, M. Mubeen, M. Zia-Ul-Haq, S. Ahmad, S. Ercisli, H. Z. E. Jaafar, Normalized Difference Vegetation Index as a Tool for Wheat Yield Estimation: A Case Study from Faisalabad, Pakistan, Sci. World J. 2014 (2014) 1–8.

[20] Y. Zhu, X. Yao, Y. Tian, X. Liu, W. Cao, Analysis of common canopy vegetation indices for indicating leaf nitrogen accumulations in wheat and rice, Int. J. Appl. Earth Obs. Geoinf. 10 (2008) 1–10.

[21] Q. Cao, Y. Miao, G. Feng, X. Gao, F. Li, B. Liu, S. Yue, S. Cheng, S. L. Ustin, R. Khosla, Active canopy sensing of winter wheat nitrogen status: An evaluation of two sensor systems, Comput. Electron. Agric. 112 (2015) 54–67.

[22] A. de Lara, T. Mieno, J. D. Luck, L. A. Puntel, Predicting site-specific economic optimal nitrogen rate using machine learning methods and on-farm precision experimentation, Precis. Agric. 24 (2023) 1792–1812.

[23] Agrosat website.
URL `https://www.agrosat.it`

[24] Agrosat article.
URL https://www.cnr.it/it/nota-stampa/n-7905/agrosat-l-agricoltura-di-precisione-con-lo-smarthphone

[25] F. S. Santaga, P. Benincasa, P. Toscano, S. Antognelli, E. Ranieri, M. Vizzari, Simplified and Advanced Sentinel-2-Based Precision Nitrogen Management of Wheat, Agronomy 11 (6) (2021) 1156.

[26] A. Cisternino, L. Incrocci, L. Lulli, M. Mariotti, Redazione del piano di concimazione (2010).

[27] Agricolus nitrogen prescription maps.
URL https://www.agricolus.com/en/prescription-maps-for-nitrogen-fertilization/

[28] T. Roßberg, M. Schmitt, A Globally Applicable Method for NDVI Estimation from Sentinel-1 SAR Backscatter Using a Deep Neural Network and the SEN12TP Dataset, J. Photogramm. Remote Sens. 91 (3) (2023) 171–188.

[29] A. Maltese, M. Cannarozzo, F. Capodici, G. L. Loggia, T. Santangelo, A sensitivity analysis of a surface energy balance model to LAI, Proc. SPIE 7104 (2008).

[30] G. A. Wood, J. P. Welsh, R. J. Godwin, Real-time measures of canopy size as a basis for spatially varying nitrogen applications to winter wheat sown at different seed rates, Biosyst. Eng. 84 (4) (2003) 513–531.

[31] Sentinel-1.
URL https://www.esa.int/Applications/Observing_the_Earth/Copernicus/Sentinel-1

[32] Sentinel-2.
URL https://www.esa.int/Applications/Observing_the_Earth/Copernicus/Sentinel-2

[33] Sentinel application platform (snap).
URL https://step.esa.int/main/download/snap-download/

[34] X. Yuan, G. Shi, L. Jianfang, A review of deep learning methods for semantic segmentation of remote sensing imagery, Expert Syst. Appl. (2021).

[35] A. Odena, V. Dumoulin, C. Olah, *Deconvolution and Checkerboard Artifacts* (2016).
URL https://distill.pub/2016/deconv-checkerboard/?ref=mlq-ai

[36] H. Zhao, O. Gallo, I. Frosio, Loss functions for image restoration with neural networks, IEEE Trans. Comput. Imaging 3 (2017) 47–57.

[37] D. P. Kingma, J. Ba, Adam: a method for stochastic optimization, Preprint at arXiv (2014).
URL https://arxiv.org/abs/1412.6980

[38] G. Hayman, J. W. Redhead, M. Brown, E. Pinnington, F. Gerard, M. Brown, W. Fincham, E. L. Robinson, C. Huntingford, R. F. Pywell, A framework for improved predictions of the climate impacts on potential yields of UK winter wheat and its applicability to other UK crops, Clim. Serv. 34 (2024).

[39] M. Abichou, Modélisation de l'architecture 4D du blé: identification des patterns dans la morphologie, la sénescence et le positionnement spatial des organes pour une large gamme de situations de croissance, Ph.D. thesis, PhD Thesis (2016).

[40] D. T. Stokes, R. Sylvester-Bradley, R. Clare, R. K. Scott, J. Hopkinson, G. F. J. Milford, S. E. Salmon, An integrated approach to nitrogen nutrition for wheat, HGCA Project Report (1998).

[41] E. Bériaux, F. Waldner, F. Collienne, P. Bogaert, P. Defourny, Maize Leaf Area Index Retrieval from Synthetic Quad Pol SAR Time Series Using the Water Cloud Model, Remote Sens. 7 (2015) 16204–16225.

[42] X. Lu, X. Wang, Z. Yang, Leaf area index estimation from the time-series SAR data using the AIEM-MWCM model, Int. J. Digit. Earth 16 (2) (2023) 4385–4403.

MOX Technical Reports, last issues

Dipartimento di Matematica
Politecnico di Milano, Via Bonardi 9 - 20133 Milano (Italy)

72/2024 Patanè, G.; Bortolotti, T.; Yordanov, V.; Biagi, L. G. A.; Brovelli, M. A.; Truong, A. Q; Vantini, S.
An interpretable and transferable model for shallow landslides detachment combining spatial Poisson point processes and generalized additive models

71/2024 Zhang, L.; Pagani, S.; Zhang, J.; Regazzoni, F.
Shape-informed surrogate models based on signed distance function domain encoding

70/2024 Panzeri, L.; Fumagalli, A.; Longoni, L.; Papini, M.; Diego, A.
Sensitivity analysis with a 3D mixed-dimensional code for DC geoelectrical investigations of landfills: synthetic tests

69/2024 Galliani, G.; Secchi, P.; Ieva, F.
Estimation of dynamic Origin–Destination matrices in a railway transportation network integrating ticket sales and passenger count data

68/2024 Gambarini, M.; Ciaramella, G.; Miglio, E.
A gradient flow approach for combined layout-control design of wave energy parks

Galliani, G.; Secchi, P.; Ieva, F.
Estimation of dynamic Origin–Destination matrices in a railway transportation network integrating ticket sales and passenger count

65/2024 Possenti, L.; Vitullo, P.; Cicchetti, A.; Zunino, P.; Rancati, T.
Modeling Hypoxia Induced Radiation Resistance and the Impact of Radiation Sources

64/2024 Cavazzutti, M.; Arnone, E.; Ferraccioli, F.; Galimberti, C.; Finos, L.; Sangalli, L.M.
Sign-Flip inference for spatial regression with differential regularization

63/2024 Vitullo, P.; Franco, N.R.; Zunino, P.
Deep learning enhanced cost-aware multi-fidelity uncertainty quantification of a computational model for radiotherapy

62/2024 Roknian, A.A.; Scotti, A.; Fumagalli, A.
Free convection in fractured porous media: a numerical study